Article

Erosion Resistance of $BaZrO_3$-Y_2O_3 Two-Phase Crucibles against Highly Active Ti_2Ni Alloys

Qisheng Feng [1], Shaowen Deng [1], Houjin Liao [1], Chenxi Liu [1], Pengyue Gao [1,2], Enhui Wang [3], Xinmei Hou [3,*], Guangyao Chen [1,2,*] and Chonghe Li [1,2,*]

[1] State Key Laboratory of Advanced Special Steel & Shanghai Key Laboratory of Advanced Ferrometallurgy & School of Materials Science and Engineering, Shanghai University, Shanghai 200072, China; fengqisheng@shu.edu.cn (Q.F.); dengshaowen@shu.edu.cn (S.D.); hjliao@shu.edu.cn (H.L.); lcxxx@shu.edu.cn (C.L.); gaopengyue@shu.edu.cn (P.G.)
[2] Shanghai Special Casting Engineering Technology Research Center, Shanghai 201605, China
[3] Institute for Carbon Neutrality, University of Science and Technology Beijing, Beijing 100083, China; wangenhui@ustb.edu.cn (E.W.)

* Corresponding author. E-mail: houxinmeiustb@ustb.edu.cn (X.H.); cgybless1@shu.edu.cn (G.C.); chli@staff.shu.edu.cn (C.L.)

Received: 29 June 2024; Accepted: 19 August 2024; Available online: 22 August 2024

ABSTRACT: In this paper, (100-m) $BaZrO_3$-mY_2O_3 (m = 0, 20, 25, 33, 50, 100) crucibles were prepared, respectively. Then, the effect of crucible composition on the interaction between crucibles and highly active titanium alloys (Ti_2Ni) was investigated. The degree of the erosion resistance of crucibles was compared before and after melting as well as the contaminated extent of the alloys. The results show that the two-phase crucibles consisting of $BaZr_{1-x}Y_xO_{3-\delta}$ and $Y_2O_3(ZrO_2)$, could be prepared after adding Y_2O_3 into the $BaZrO_3$ crucible. As the amount of Y_2O_3 addition in the crucible was increased, the erosion resistance of the crucible to the alloy melt was gradually improved. The two-phase crucible with 50 wt.% Y_2O_3 addition exhibited the best erosion resistance with a 7 μm thick erosion layer, which was at the same level compared to the pure Y_2O_3 crucible (6.5 μm). However, the inclusion contaminants caused by this two-phase crucible were smaller than those of the pure Y_2O_3 crucible. This study provided a theoretical basis for further research on the preparation of highly stable crucibles for melting highly active titanium alloys.

Keywords: $BaZrO_3$; Y_2O_3; Crucible; Ti_2Ni alloys; Vacuum induction melting

1. Introduction

Titanium alloys have been extensively used in high-performance and advanced engineering fields like aerospace, marine, military and biomedical due to their excellent and well-balanced properties [1–3]. Additionally, the superior properties of the alloys in practical applications are often highly sensitive to their metallurgy quality.

Generally, Vacuum Arc Remelting (VAR), Plasma Arc Melting (PAM), Electron Beam Melting (EBM) and Induction Skull Melting (ISM) are commonly used to prepare the titanium alloys [4,5]. However, unavoidable heat loss and significant elemental segregation intensify the preparation cost due to forced water-cooling and repeated melting [5]. In contrast, Vacuum Induction Melting (VIM) in a refractory crucible has been considered low-cost for the one-time preparation of alloys. It is not only forced water-cooling that can be avoided, but also electromagnetic stirring that can achieve the rapid homogenization of alloy melts [6,7]. However, the highly reactive alloy melts will easily react with the refractory to contaminate the alloy melts. Thus, to select a highly stable crucible refractory is the key for the successful use of the VIM method [8].

Currently, the oxide refractories have been extensively investigated, including MgO, Al_2O_3, ZrO_2, CaO, and Y_2O_3. However, these oxide refractory crucibles are proved to be somewhat problematic in the process of melting titanium alloys [9,10]. Among these refractories, only Y_2O_3 refractory has been successfully applied in the investment casting of titanium alloys. However, its application for melting titanium alloys still faces some technical problems due to poor thermal shock resistance [11,12]. Recently, the perovskite-structured refractory has attracted widespread attention due

https://doi.org/10.35534/htm.2024.10003

to the high thermodynamic stability and high melting points, such as $CaZrO_3$, $SrZrO_3$, and $BaZrO_3$ [13–16]. Additionally, the $BaZrO_3$ refractory has garnered significant attention in numerous studies for melting various types of titanium alloys. For example, Gao et al. prepared TiNi alloys in a $BaZrO_3$ crucible, which achieved a higher shape memory rate and fatigue life than that prepared using a graphite crucible [17]. In addition, laboratory-grade TiAl alloys were prepared using the $BaZrO_3$ crucible in comparison with the Al_2O_3 and MgO crucibles, respectively. It revealed that the $BaZrO_3$ refractory caused the least contamination to the alloy melt [18]. Furthermore, a pilot-scale preparation of TiAl alloys was also achieved by using home-made 25 kg $BaZrO_3$ crucible [19]. However, Chen et al. presented that the stability of the $BaZrO_3$ crucible was insufficient during the melting of Ti-rich alloys [20]. Therefore, improving the stability of $BaZrO_3$ crucibles is necessary to expand their application in the preparation of titanium alloys.

Researchers have reported that the stability of $BaZrO_3$ refractory could be significantly improved by doping Y ions. Chen et al. compared the melting performance of $BaZrO_3$ and Y-doped $BaZrO_3$ crucibles in contact with the TixNi alloy melts, and confirmed that the Y-doped $BaZrO_3$ refractory exhibited superior erosion resistance to the alloy melts [21]. Also, a similar experimental result was obtained by Kang's study [22]. In addition, considering the high-temperature stability of Y_2O_3 refractory, and the Y-doped $BaZrO_3$ solid solution phase, it could be generated by mixing and sintering the Y_2O_3 and $BaZrO_3$ composite refractory. Chen et al. presented that the $BaZrO_3$-Y_2O_3 two-phase refractory exhibited good stability. The performance for melting TiAl alloys had revealed that it had a better stability than that of the pure Y_2O_3 refractory [23]. However, due to the inadequacy of Ti activity in TiAl alloys, the advantage of the $BaZrO_3$-Y_2O_3 two-phase crucible for melting Ti-rich alloys could not be fully reflected. Subsequently, Hou et al. [24] used the same $BaZrO_3$-Y_2O_3 two-phase crucible for melting Ti_2Ni alloy with higher Ti activity. The results preliminarily demonstrated that the $BaZrO_3$-Y_2O_3 two-phase crucible exhibits better erosion resistance compared to the $BaZrO_3$ crucible. However, the effects of different content of Y_2O_3 additions on the phase composition and microstructure of $BaZrO_3$-Y_2O_3 two-phase crucible have not been investigated. The impact of Y_2O_3 addition on Ti_2Ni alloy is also unknown, such as the content of inclusions. Therefore, it is necessary to further investigate the performance of $BaZrO_3$-Y_2O_3 two-phase crucibles with different Y_2O_3 additions for melting Ti-rich alloys.

In this paper, the $BaZrO_3$-Y_2O_3 two-phase crucibles with different content of Y_2O_3 additions were prepared, and their phase composition and microstructure were further investigated. The interaction of $BaZrO_3$-Y_2O_3 two-phase crucibles with Ti-rich Ti_2Ni alloys was studied in comparison with the pure $BaZrO_3$ and Y_2O_3 crucibles. This study was devoted to obtaining high-quality Ti_2Ni alloy ingot to lay the foundation for the preparation of A_2B-type Ti_2Ni hydrogen storage materials.

2. Experimental Procedure

2.1. Raw Materials

The crucible raw materials were $BaZrO_3$ powder (purity > 99.9%, size 13 μm, Shandong Haoyao New Material Co., Ltd., Jinan, China) and commercial Y_2O_3 powder (purity > 99.9%, size 5 μm, Sinopharm Chemical Reagent Co., Ltd., Shanghai, China). The titanium sponge (purity > 99.9%) and nickel plate (purity > 99.9%) were used to prepare the Ti_2Ni alloys.

2.2. Preparation of the Crucibles

Firstly, $BaZrO_3$ and Y_2O_3 were mixed into four kinds of powders (Y20~Y50) according to different weight ratios, as shown in Table 1. These powders (Y20~Y50) were mixed with ethanol, respectively, and ball-milled in a concrete mixer at 300 rpm/min for 6 h, then dried at 120 °C for 12 h. The dried powders were fabricated into the crucible green body in a U-shape steel mandrel using the cold isostatic pressing with 150 MPa for 3 min, which was followed by sintering treatment at 1750 °C for 6 h in a silicon-molybdenum rod sintering furnace. Meanwhile, the $BaZrO_3$ (BZ) and Y_2O_3 (Y100) crucibles were prepared in the same method. Before the melting, small pieces of the crucible were cut out and polished with ethanol in a metallographic polishing machine, which were used to analyze the microstructure.

Table 1. The crucible composition with different ratios of Y_2O_3 and $BaZrO_3$ (wt.%).

Composition	**Number of Crucibles**					
	BZ	**Y20**	**Y25**	**Y33**	**Y50**	**Y100**
Y_2O_3	0	20	25	33	50	100
$BaZrO_3$	100	80	75	67	50	0

2.3. Melting Experiment

A molar ratio of titanium sponge to nickel plate of 2:1 was adopted to prepare Ti_2Ni master alloys in a water-cooled copper induction furnace. The crucible for melting was inserted into a VIM furnace (WZG-2, Jinzhou Oriental Metallurgical Technology Research Co., Ltd., Shenzhen, China) and filled with Al_2O_3 ramming mass to avoid the leakage of alloy melt. Then, 75 g Ti_2Ni alloy was put in the crucible. The furnace was evacuated to 10^{-2} Pa and backfilled with high purity argon. The temperature was raised to 1600 °C holding for 3 min, and then it was poured into a graphite crucible to obtain alloy ingot. Three melts of Ti_2Ni alloy were carried out using each crucible. The same melting process was performed for six different crucibles (BZ~Y100). The flowchart of the melting experiment was shown in Figure 1.

Figure 1. Schematic diagram of the experimental procedure.

2.4. Analysis Method

For the crucibles before and after melting, the phase compositions were identified using X-ray diffraction (XRD, D8 Advance, Bruker, Ettlingen, Germany) with a Cu-Kα source operated at 40 KV and 30 mA (0.02 °, 4 °/min, variable slit). The microstructure of all samples was characterized by scanning electron microscopy (SEM, Gemini 300, Oberkochen, Germany) with energy dispersive spectroscopy (EDS, 50 mm^2, X-Max N 50, Oxford, UK). The contamination of Ti_2Ni alloy melts by crucibles was investigated using inductively coupled plasma atomic emission spectrometry (ICP-AES 710-ES, Palo Alto, CA, USA) and O/N/H analyzer (LECO TC600, St. Joseph, MI, USA).

3. Results and Discussion

3.1. Phase and Microstructure Analysis of the Crucibles

Figure 2 shows the XRD patterns of BZ~Y100 crucibles after sintering. As can be seen in Figure 2a, the BZ crucible consisted of cubic $BaZrO_3$ (ICDD PDF# 00-006-0399) and tetragonal ZrO_2 (ICDD PDF# 00-080-2155) phases. Our previous study [23] revealed that the volatilization of BaO during the preparation of $BaZrO_3$, resulted in the residual of the second phase ZrO_2. When the adding amount of Y_2O_3 addition ranged from 20~50 wt.% (Y20~Y50), the ZrO_2 phase disappeared. In addition, these crucibles consisted of $BaZrO_3$ and cubic Y_2O_3 (ICDD PDF# 00-043-1036), respectively. From Figure 2b, it can be seen that the characteristic peaks of $BaZrO_3$ and Y_2O_3 were shifted to lower and higher angles in the Y20~Y50 crucibles, respectively. It is because Zr^{4+} (0.72 Å) ions in $BaZrO_3$ crystal lattice were partially replaced by Y^{3+} (0.90 Å) ions, and Y^{3+} ions in Y_2O_3 crystal lattice were partially substituted by Zr^{4+} ions, which could be further verified using the following formulae [25]:

$$2d\sin\theta = n\lambda(n = 1, 2, 3 \cdots) \tag{1}$$

$$d = a/\sqrt{(h^2 + k^2 + l^2)} \tag{2}$$

where d is the interplanar spacing; λ is the X-ray wavelength; a is the lattice constant of the cubic structure; h, k and l are the Miller indices corresponding to the diffraction peak. Combining Equations (1) and (2) shows that the substitution of Y^{3+} ions for Zr^{4+} ions led to an increase in the lattice constant a, and an accompanying increase in the interplanar spacing d, which finally resulted in a decrease in θ, i.e., a leftward shift of diffraction peak. The space group of cubic $BaZrO_3$ is Pm-3m, and Ba^{2+} ions with coordination number 12 and Zr^{4+} ions with coordination number 6 correspond to ionic radii of 1.61 Å and 0.72 Å, respectively [26]. The space group of cubic Y_2O_3 is Ia-3, and the ionic radius corresponding to Y^{3+} ions with coordination number 6 is 0.90 Å [26]. The relative ionic radius difference between Zr^{4+} and Y^{3+} ions is about 13%, which is less than 15%, indicating that they can be substituted for each other [27].

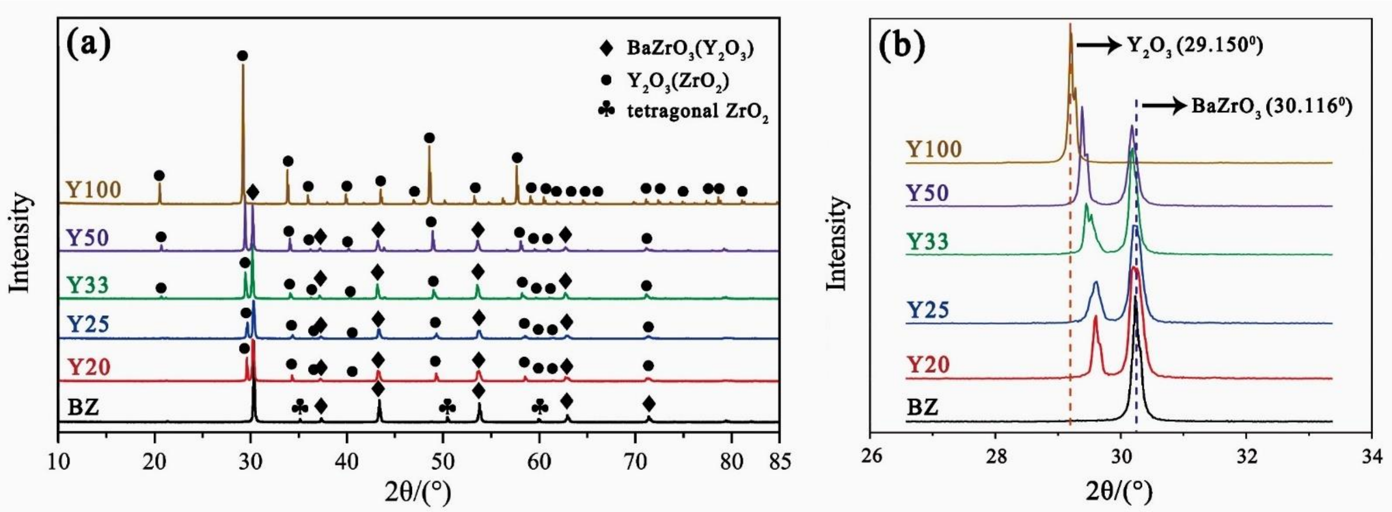

Figure 2. (**a**) XRD patterns of all crucibles after sintering; (**b**) magnified pictures over the 2θ ranges of 28~32° showing Y_2O_3 and $BaZrO_3$ peaks.

Figure 3 shows the inner microstructure of BZ~Y100 crucibles after grinding and polishing. From Figure 3a, it can be seen that the BZ crucible consisted of light gray (spot 1) and gray (spot 2) substances with the appearance of some pores, respectively. EDS results in Table 2 indicated that spots 1 and 2 were $BaZrO_3$ and ZrO_2 phases, respectively. After adding 20 wt.% Y_2O_3 into $BaZrO_3$ (Y20 crucible, Figure 3b), the amount of gray substance (spot 4), which was dispersed throughout the crucible matrix, exhibited a significant increase trend and became Y_2O_3 with ZrO_2 in solid solution. EDS results indicated spots 3 and 4 were $BaZr_{1-x}Y_xO_{3-\delta}$ and $Y_2O_3(ZrO_2)$, respectively. According to the phase diagram of ZrO_2-Y_2O_3 system [28] shown in Figure 4a, at 1750 °C, the solubility limit of ZrO_2 in cubic Y_2O_3 is 12.71 at. % (atomic percent) and the solubility limit of Y_2O_3 in tetragonal ZrO_2 is 4.25 at. %. At the same time, the cubic solid solution formed by cubic ZrO_2 and cubic Y_2O_3 ranges from 11.11 at. % to 67.62 at. %. The values of Y/(Zr + Y) (spots 4, 6, 8, and 10) in Table 2 are basically consistent with calculated results in Figure 4a. According to the isothermal section of the BaO-ZrO_2-Y_2O_3 system [28] at 1750 °C (Figure 4b), the solubility limit of Y_2O_3 in $BaZrO_3$ is 24.43 at. %. The values of Ba/(Zr + Y) and Y/(Zr + Y) (spots 3, 5, and 7) in Table 2 are fully consistent with calculated results in Figure 4b. For the EDS results of spot 9, the values of Ba/(Zr + Y) and Y/(Zr + Y) differ significantly from other results (spots 3, 5, and 7), which is considered to be due to measurement errors. It was caused by the solid solution of Y_2O_3 into $BaZrO_3$ and ZrO_2 into Y_2O_3, which was consistent with the shifts of observed characteristic peaks in Figure 2b. In addition, through comparison, it can be found that the number of pores in Figure 3b is significantly less than that in Figure 3a. Apparently, the Y_2O_3 addition had two obvious effects. One was to consume the ZrO_2 phase in the crucible, leading to the formation of a more stable $Y_2O_3(ZrO_2)$ phase according to the solid solution effect [24]. The other was to increase the densification of the crucible due to the effect of solid solution sintering. As the amount of Y_2O_3 addition increased from 25~50 wt.% (Y25~Y50 crucibles), the different grains were evenly distributed, and the $Y_2O_3(ZrO_2)$ phase obviously increased with the growth of Y_2O_3 additions, as shown in Figure 3c–e. In addition, the number of pores in crucibles was further decreased, indicating that an increased amount of Y_2O_3 addition could continue to improve the densification of $BaZrO_3$-Y_2O_3 two-phase crucibles. From Figure 3f, it can be seen that only Y_2O_3 phase (spot 11) could be observed, and a large number of pores were dispersed in the Y100 crucible. The solid solution between Y_2O_3, ZrO_2 and $BaZrO_3$ during sintering could be described as follows:

$$\mathrm{BaZrO_3 + Y_2O_3 \xrightarrow{1750\,°C,6\,h} BaZr_{1-x}Y_xO_{3-\delta}} \tag{3}$$

$$\mathrm{Y_2O_3 + ZrO_2 \xrightarrow{1750\,°C,6\,h} Y_2O_3(ZrO_2)} \tag{4}$$

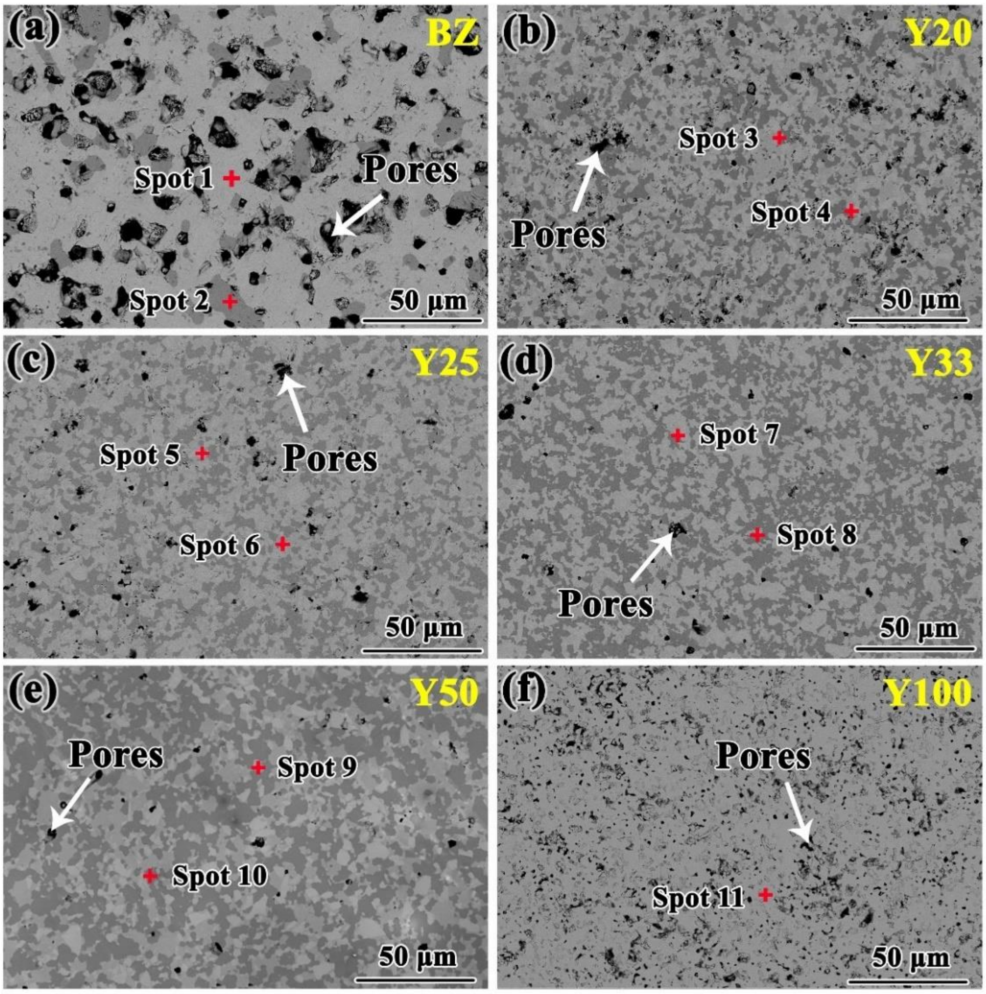

Figure 3. SEM pictures (BSE mode) of bottom wall of all crucibles after grinding and polishing: (**a**) BZ crucible; (**b**) Y20 crucible; (**c**) Y25 crucible; (**d**) Y33 crucible; (**e**) Y50 crucible; (**f**) Y100 crucible.

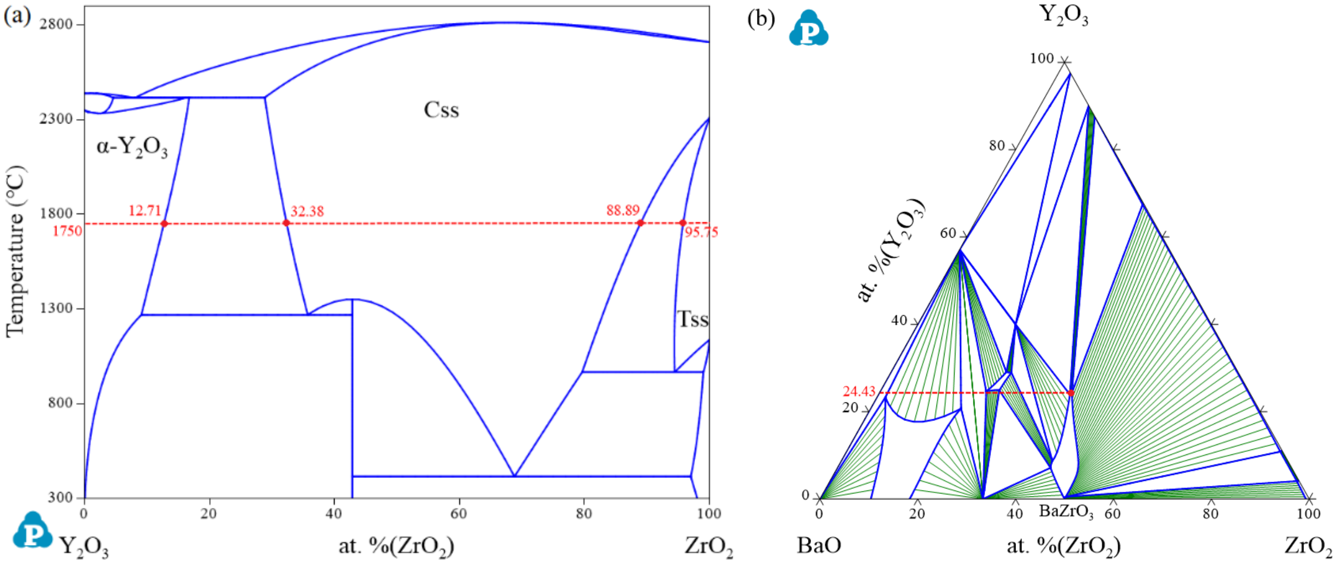

Figure 4. (**a**) Calculated phase diagram of ZrO_2-Y_2O_3 system (Css---Cubic structure solid solution; Tss---Tetragonal structure solid solution) [28]; (**b**) Calculated isothermal section of BaO-ZrO_2-Y_2O_3 system at 1750 °C [28].

Table 2. EDS results of points 1~11 shown in Figure 3.

Point	Element Content (at. %)				Possible Phase	Ba/(Zr + Y)	Y/(Zr + Y)
	Ba	Zr	Y	O			
1	21.89	22.13	/	56.07	$BaZrO_3$	0.99	0
2	0.11	33.12	/	66.77	ZrO_2	≈0	0
3	22.83	19.51	2.44	55.22	$BaZr_{1-x}Y_xO_{3-\delta}$	1.04	0.11
4	/	16.72	18.44	64.84	$Y_2O_3(ZrO_2)$	0	0.52
5	21.23	19.50	3.15	56.12	$BaZr_{1-x}Y_xO_{3-\delta}$	0.94	0.14
6	/	16.76	22.43	60.81	$Y_2O_3(ZrO_2)$	0	0.57
7	24.81	23.10	2.84	49.25	$BaZr_{1-x}Y_xO_{3-\delta}$	0.96	0.11
8	/	11.44	25.39	63.14	$Y_2O_3(ZrO_2)$	0	0.69
9	15.68	18.63	7.67	58.01	$BaZr_{1-x}Y_xO_{3-\delta}$	0.60	0.29
10	/	3.54	20.25	76.21	$Y_2O_3(ZrO_2)$	0	0.85
11	/	/	54.32	45.68	Y_2O_3	0	1

To further investigate the effect of Y_2O_3 additions on the sintering behavior of $BaZrO_3$-Y_2O_3 two-phase crucibles, ImageJ software was used to analyze the percentage of pore areas, as shown in Figure 5. Three pictures of each crucible sample were measured and the average percentage of pore areas was calculated. From Figure 5a, it can be seen that the percentage of pore areas in BZ crucible reached 18.2 ± 2.1%. It is because the $BaZrO_3$ refractory with a high melting point (nearly 2650 °C) was difficult to densify at 1750 °C [23]. Additionally, the presence of ZrO_2 secondary phase partially inhibited the growth of $BaZrO_3$ grains, leading to the residual of pores. After adding Y_2O_3, from Figure 5b–e, it can be seen that the percentage of pore area in Y20~Y50 crucibles exhibited a significant decrease trend from 3.5 ± 0.6% to 1.2 ± 0.3%, respectively. The lower porosity could have a good effect to resist the erosion of alloy melts. In the BaO-Y_2O_3 phase diagram [28], all eutectic reaction temperatures including the liquid phase are greater than 1750 °C. When sintered at 1750 °C, Y^{3+} replaces Zr^{4+} in $BaZrO_3$, resulting in oxygen vacancies [29]. These factors have led to the decrease in the percentage of pore area. For the Y100 crucible, its percentage of pore area also reached 8.2 ± 1.1%, as shown in Figure 5f. Apparently, the melting point of Y_2O_3 (2410 °C) [23] was lower than that of $BaZrO_3$ (2650 °C), indicating that the sintering performance of Y_2O_3 was better than that of $BaZrO_3$ under the same conditions.

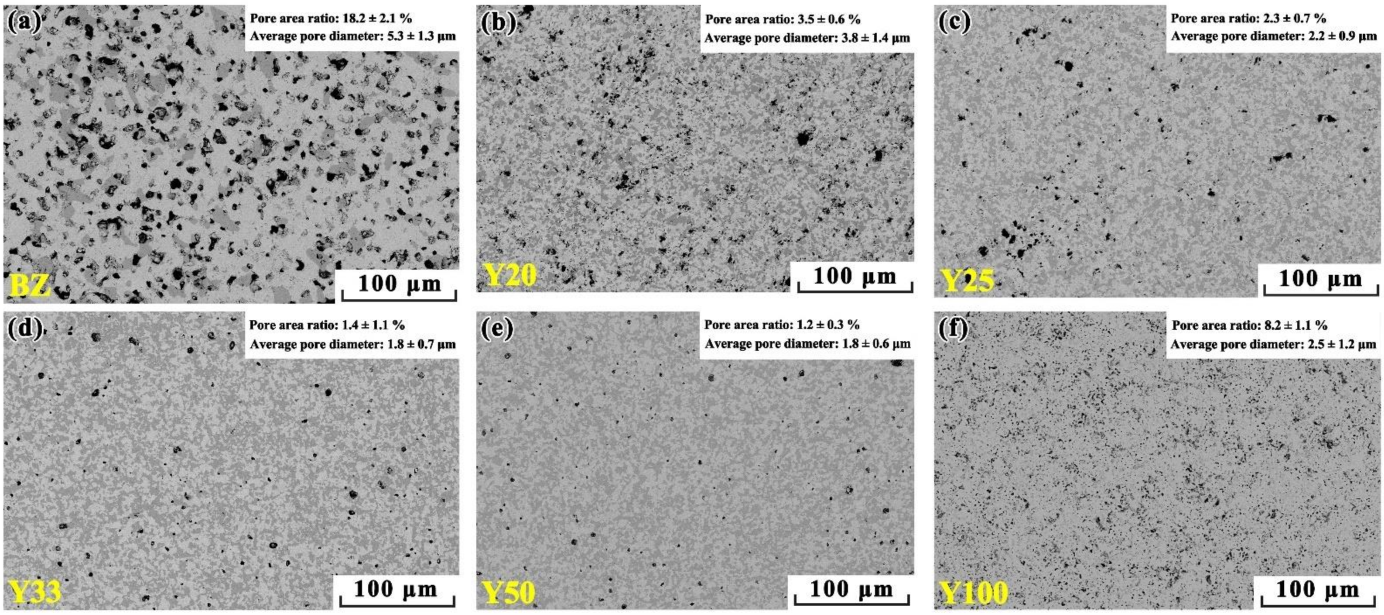

Figure 5. SEM pictures of the inner of all crucibles and the measured porosity ratio: (**a**) BZ crucible; (**b**) Y20 crucible; (**c**) Y25 crucible; (**d**) Y33 crucible; (**e**) Y50 crucible; (**f**) Y100 crucible.

3.2. Interaction between the Crucibles and Ti_2Ni Alloy Melts

The phases of the inner surfaces of BZ~Y100 crucibles after the melting of Ti_2Ni alloys were characterized by XRD, as shown in Figure 6. For the BZ crucible, not only no new phase was observed, but also the disappearance of ZrO_2 characteristic peaks. The glassy phase is possible, but not easily detected by XRD, which is mainly sensitive to crystalline phases. Chen et al. [30] proposed that the interaction of refractory crucible with Ti melt was caused by physical dissolution of the refractory, it could be confirmed that the Ti_2Ni alloy melt dissolved the ZrO_2 refractory on the surface of the $BaZrO_3$ crucible. The loose and non-uniform structure of the crucible surface is due to the partial dissolution of the $BaZrO_3$ refractory. For the Y100 crucible, no new phase was observed compared to the original crucible in Figure 2a, indicating that the interaction of Ti_2Ni alloy melt with Y_2O_3 crucible did not generate any new crystalline product but a glassy phase may exist. For the Y20~Y50 crucibles after melting, there was no appearance of new interaction product on their surfaces in comparison with the original crucibles in Figure 2a.

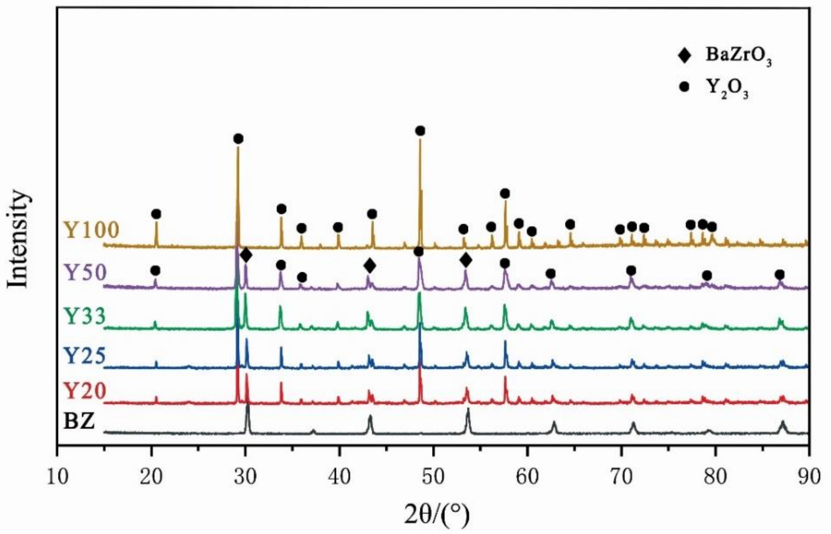

Figure 6. XRD patterns of the inner surface of all crucibles after the melting of Ti_2Ni alloys.

Figure 7 shows the cross-sections of the bottom wall of BZ~Y100 crucibles after melting Ti_2Ni alloys. As shown in Figure 7a, the internal structure of the BZ crucible was damaged due to the infiltration of alloy melts. The generated thickness of the erosion layer was about 658 μm. For the Y20 crucible, the thickness of the erosion layer had a significant decrease to 142 μm, as shown in Figure 7b. As the increase of Y_2O_3 content in the $BaZrO_3$ crucible, the thickness of the erosion layer was further decreased. For Y25~Y50 crucibles (Figure 7c–e), it ranged from 65 to 7 μm. However, for the Y100 crucible (Figure 7f), the thickness of the erosion layer was only 6.5 μm.

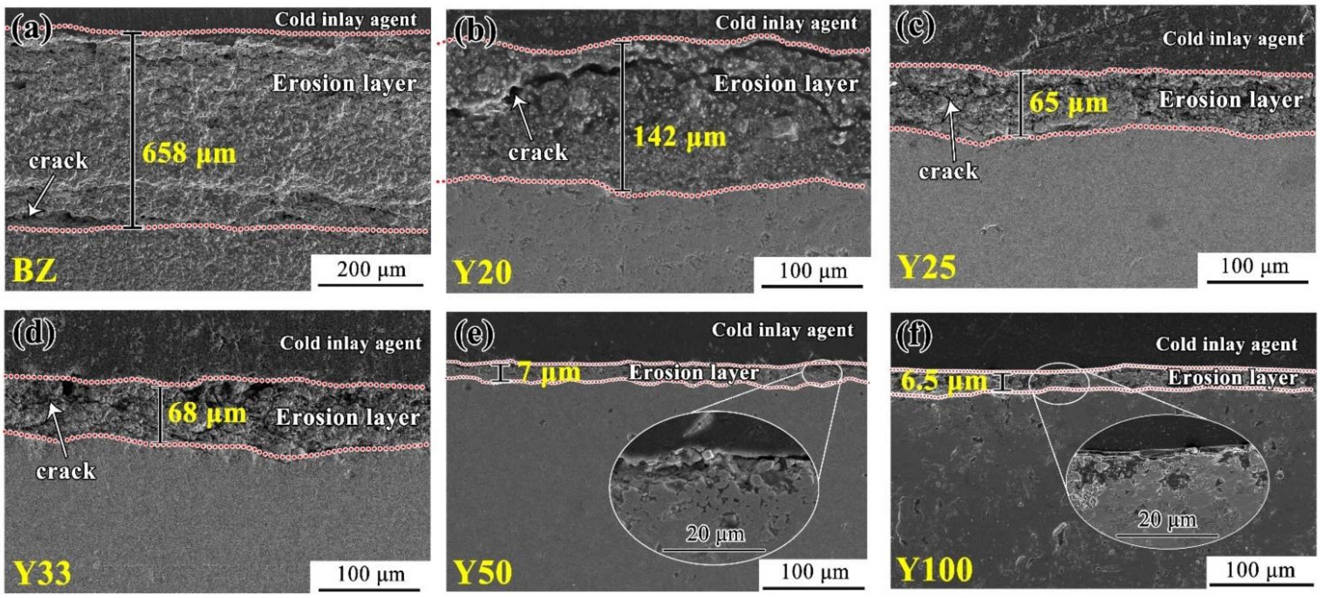

Figure 7. SEM pictures of the cross-section of bottom wall of all crucibles after melting Ti_2Ni alloys: (**a**) BZ crucible; (**b**) Y20 crucible; (**c**) Y25 crucible; (**d**) Y33 crucible; (**e**) Y50 crucible; (**f**) Y100 crucible.

The magnified pictures of the erosion layers of BZ, Y20, Y50, and Y100 crucibles are shown in Figure 8. From Figure 8(a1), it can be seen that the erosion layer of BZ crucible exhibited a clear layered structure, which showed a loose and porous phenomenon. The corresponding mapping analysis indicated that only Ba and Zr elements exist in the erosion layer, and there is no residue of alloy melts, as shown in Figure 8(a2). In addition, the EDS result of spot A

(Table 3) showed that BaO phase was observed. In our previous studies [23], we had revealed that the decomposition of $BaZrO_3$ refractory in titanium alloy melts could cause the evaporation of BaO and the Zr and O elements into alloy melts. The same phenomenon was also observed in the melted Y20 crucible, as shown in Figure 8(b1,b2). In the Y50 crucible (Figure 8(c1,c2)), the enrichment of BaO disappeared as the decreasing of $BaZrO_3$ content. In addition, the Zr elements caused by the dissolution of $BaZrO_3$ would be partially dissolved into Y_2O_3, which will reduce the Zr pollution to the alloy. As can be seen from Figure 8(d1,d2), the Y100 crucible also did not react with alloy melt and was able to resist the mechanical scouring of alloy melt, indicating that Y_2O_3 refractory has good thermodynamic stability. However, the Y100 crucible has an obvious disadvantage, the Y generated by the dissolution of Y_2O_3 reacts with the O in the alloy melt to generate a large number of oxide inclusions [31].

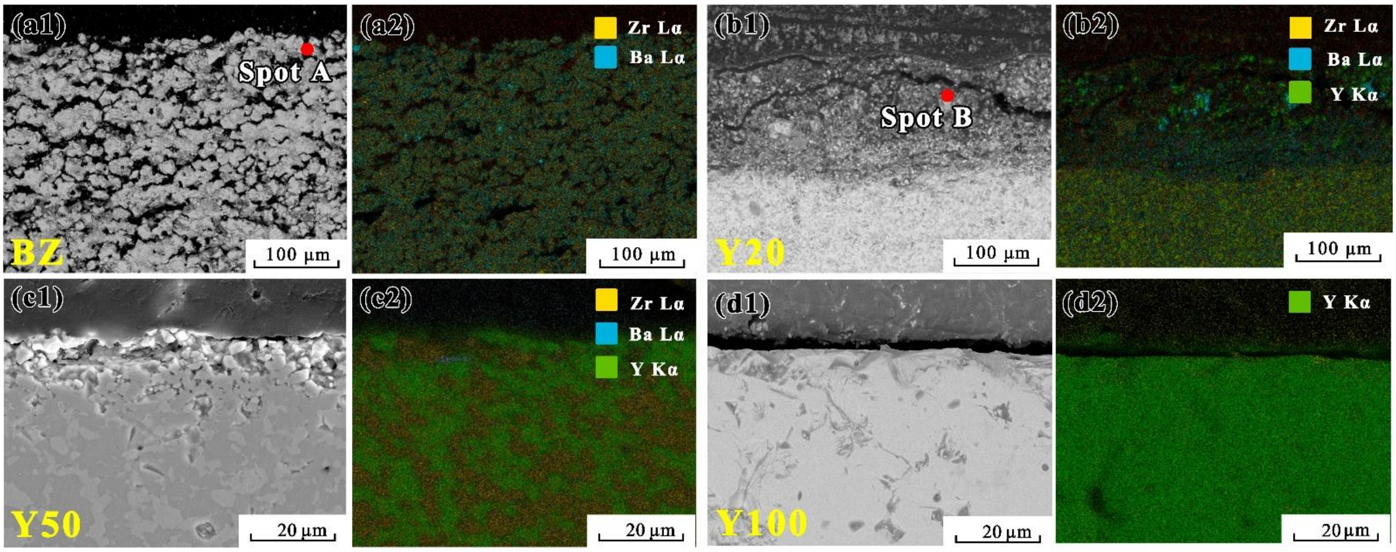

Figure 8. Localized enlargement of the erosion layers of crucibles: (**a1**) BZ crucible; (**a2**) the elemental mapping of Figure 8(a1); (**b1**) Y20 crucible; (**b2**) the elemental mapping of Figure 8(b1); (**c1**) Y50 crucible; (**c2**) the elemental mapping of Figure 8(c1); (**d1**) Y100 crucible; (**d2**) the elemental mapping of Figure 8(d1).

Table 3. EDS results of points A and B shown in Figure 8.

Point	**Element Content (at. %)**				**Possible Phase**
	Ba	**Zr**	**Y**	**O**	
A	69.51	2.28	/	27.94	BaO
B	67.58	2.28	3.57	26.57	BaO

Actually, the purity degree of titanium alloys was an important evaluation criterion for the practical application. Figure 9 shows the number of melted Ti_2Ni alloys using BZ~Y100 crucibles as well as the O, Zr, and Y element concentrations in each alloy. Figure 9a shows the change trend of O concentration. It can be seen that the O concentration exhibited a decreasing trend as the increase of melting number regardless of the type of crucibles. However, it was more obvious that the $BaZrO_3$ crucibles with Y_2O_3 addition exhibited a rapid decrease trend for the O concentration. It consisted of the analysis for the erosion layer in Figures 7 and 8. Especially, the alloy melted in the Y50 crucible, its O concentration was only 0.11 wt.% after third melting, which is basically the same as that of alloy melted in the Y100 crucible. The change trend of Zr concentration is shown in Figure 9b, it can be seen that the Zr concentration also exhibited the same change trend as the O concentration. After third melting, the Zr concentration in alloy melted with the Y50 crucible was only 0.05 wt.%, which is much lower than 0.64 wt.% in the BZ crucible. This result was in consistent with the analysis of Figure 8, where the Zr element generated by the dissolution of crucibles was partially solidified into Y_2O_3. From Figure 9c, the Y concentration in alloy exhibited a clear increasing trend with the increase of Y_2O_3 addition. The Y concentration in alloy melted in the Y100 crucible increases from 0.10 to 0.24 wt.% with the increase in melting times, which is due to the large amount of Y_2O_3 dissolution [11,12]. After third melting, the Y concentration in alloy melted in Y20~Y50 crucibles ranged from 0.08 to 0.13 wt.%, and the Y50 crucible with the highest Y concentration was only half of the Y100 crucible. Considering the contamination degree from the three elements, the Y50 crucible clearly showed the best melting performance.

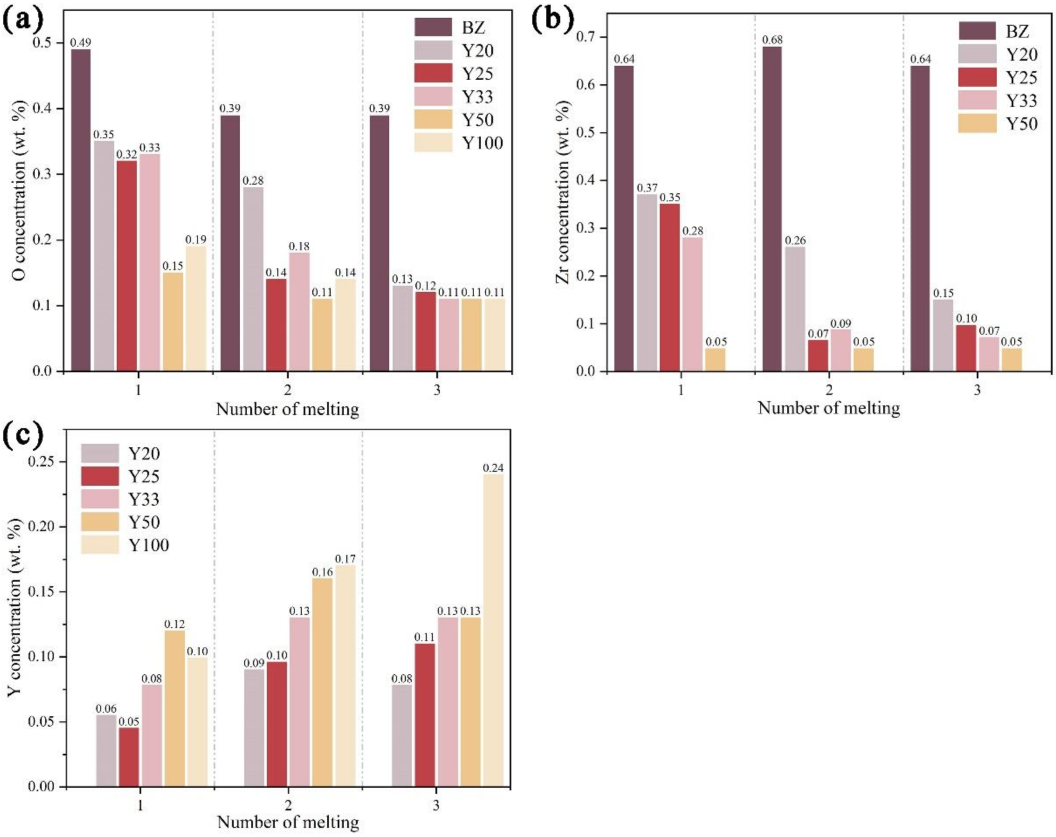

Figure 9. The O, Zr, and Y element concentrations in Ti_2Ni alloys after melting for different times using the BZ~Y100 crucibles: (**a**) O concentration; (**b**) Zr concentration; (**c**) Y concentration.

Figure 10 shows the microstructure of alloys for the third melting in BZ, Y20, Y50, and Y100 crucibles. From Figure 10(a1,a2), the alloy cooled in the BZ crucible contains some gray particles. Combined with EDS results in Table 4 (spots 1–2), the alloy matrix was Ti_2Ni and the gray particles were residual TiNi. As can be seen in Figure 10(b1), some gray and white particles appeared in the alloy cooled in the Y20 crucible. The gray particles appeared as long strips with a tendency to break off, and most of white particles were attached around gray particles. Combined with the Figure 10(b2) and EDS results (spots 3–5) in Table 4, the white particles were Y_2O_3, the alloy matrix was Ti_2Ni, which was consistent with the target composition, and the gray particles were residual TiNi. From the Ni-Ti phase diagram (Figure 11) [32], it can be seen that the Ti_2Ni alloy firstly entered the two-phase region of liquid and TiNi from the liquid-phase region during solidification process, and then underwent the peritectic reaction Liquid + TiNi → Ti_2Ni at 1258 K, and the generated Ti_2Ni was retained until room temperature. It is hypothesized that the peritectic reaction did not occur completely resulting in a small amount of TiNi remaining in solidified Ti_2Ni matrix. From Figure 10(c1,c2) and EDS results (spots 6–8) in Table 4, the same residual TiNi and inclusions Y_2O_3 were present in Ti_2Ni matrix cooled in the Y50 crucible. As the Y_2O_3 content was increased, the residual long strips of TiNi became fewer and finer, while fracture occurred, indicating that Y_2O_3 promoted this peritectic reaction. The amount and morphology of TiNi remaining in the cooled Ti_2Ni matrix in the Y100 crucible (Figure 10(d1,d2)) was basically the same as that of the Y50 crucible. The presence of Y_2O_3 inclusions was caused by the dissolution of Y_2O_3 refractory in melting process, which was facilitated by the Y100 crucible [33].

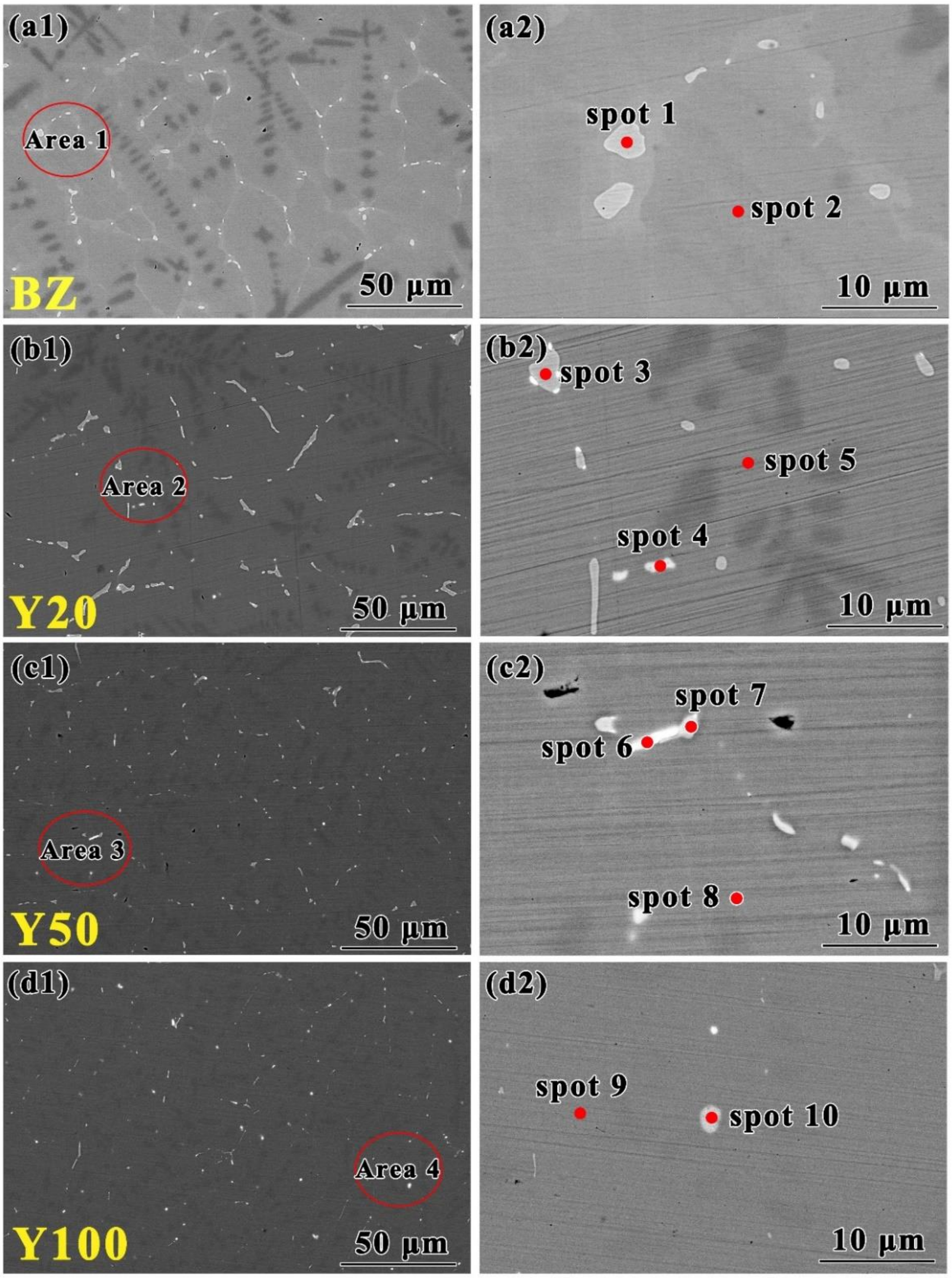

Figure 10. SEM photographs of the alloys melted in crucibles for the third melting: (**a1**) in the BZ crucible; (**a2**) the magnified image of area 1; (**b1**) in the Y20 crucible; (**b2**) the magnified image of area 2; (**c1**) in the Y50 crucible; (**c2**) the magnified image of area 3; (**d1**) in the Y100 crucible; (**d2**) the magnified image of area 4.

Table 4. EDS results of points 1~10 shown in Figure 10.

Point	Element Content (at. %)				Possible Phase
	Ti	Ni	Y	O	
1	53.49	46.51	/	/	TiNi
2	68.02	31.98	/	/	Ti_2Ni
3	55.43	44.57	/	/	TiNi
4	/	/	38.15	61.85	Y_2O_3
5	71.34	28.66	/	/	Ti_2Ni
6	29.07	11.63	18.22	41.08	Ti_2Ni, Y_2O_3
7	54.17	45.61	0.22	/	TiNi
8	66.87	33.13	/	/	Ti_2Ni
9	70.16	29.84	/	/	Ti_2Ni
10	22.02	8.34	22.65	46.99	Ti_2Ni, Y_2O_3

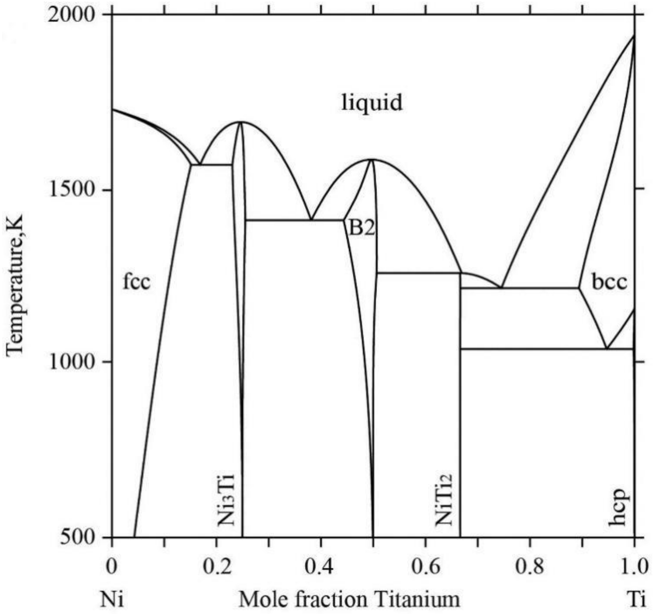

Figure 11. The Ni-Ti phase diagram [32].

3.3. Erosion Resistance Mechanism

From the above analysis, it can be seen that $BaZrO_3$-Y_2O_3 two-phase crucibles had a certain advantage in comparison with the pure BZ and Y100 crucibles. In particular, the Y50 crucible exhibited the best erosion resistance. In the following, the Y50 crucible was taken as an example to explore the mechanism by which it effectively prevents the erosion of alloy melts. With the addition of Y_2O_3, the average pore diameter of the crucible gradually decreases, and the Y50 crucible reaches the minimum value (1.8 ± 0.6 μm), as shown in Figure 5e. On the whole, combined with Figures 5 and 7, the erosion layer thickness decreased with decreasing average pore diameter, which is consistent with the Washburn model for liquid penetration into a capillary [34]:

$$h^2 = \frac{r(cos\theta)\sigma t}{2\eta} \tag{5}$$

where h is the erosion layer thickness, r is the pore radius, θ is the contact angle, σ is the surface tension, t is the interaction time, and η is the alloy melt viscosity. Although the porosity also decreases with the addition of Y_2O_3, the Y50 crucible also reaches the minimum value (1.2 ± 0.3%), the erosion layer thickness of the Y100 crucible with a porosity of 8.2 ± 1.1% is basically the same as that of the Y50 crucible. This showed that the average pore size has more influence on the erosion layer than porosity.

The erosion resistance of crucible was also affected by its thermodynamic stability and thermal shock resistance [9,35]. Figure 12 shows the Ellingham diagram of TiO_2, TiO, ZrO_2, $BaZrO_3$ and Y_2O_3. At the experimental temperature (1600 °C), the thermodynamic stability of ZrO_2, $BaZrO_3$ and Y_2O_3 was significantly higher than that of TiO_2 and TiO. Therefore, no chemical reaction occurred between BZ~Y100 crucibles and alloy melts, which was consistent with the experimental results. In $BaZrO_3$-Y_2O_3 two-phase crucibles, the presence of solid solution effects led to a further decrease in the Gibbs free energy of $BaZr_{1-x}Y_xO_{3-\delta}$ and $Y_2O_3(ZrO_2)$ [23]. Hence, compared to BZ and Y100 crucibles, the Y50 crucible had a higher thermodynamic stability. It should be noted that physical dissolution of crucible refractory was unavoidable due to mechanical scouring of the inner wall of crucible by alloy melts [36].

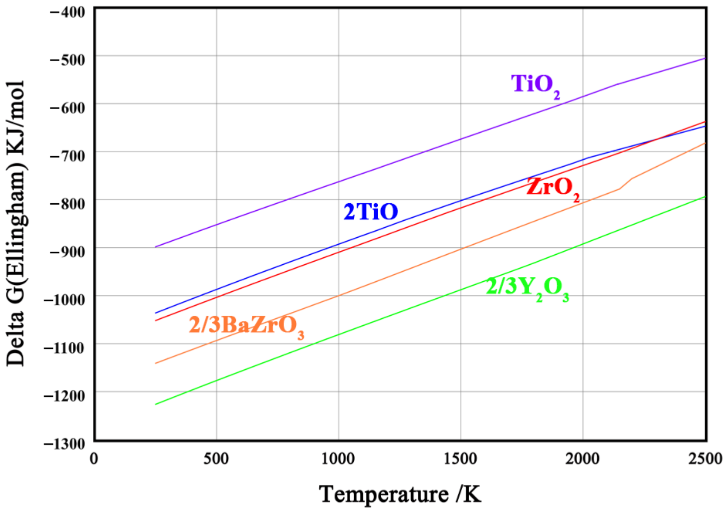

Figure 12. Gibbs free energy of formation of TiO_2, TiO, ZrO_2, $BaZrO_3$ and Y_2O_3.

Generally, crucibles with low porosity and high thermal shock resistance would have a long service life. In addition, high thermal conductivity and a low linear expansion coefficient were necessary to obtain high thermal shock resistance [37]. High thermal conductivity crucibles had smaller thermal gradients, while low linear expansion coefficient crucibles expanded less and deformed more uniformly, thus reducing thermal stresses and preventing the damage of the crucible. The thermal shock resistance of crucibles could be predicted by calculating the thermal stress resistance parameters R, the following equations [38,39]:

$$R = \frac{\sigma_f(1-\nu)}{E\alpha} \tag{6}$$

where σ_f, E, α, and ν represent the strength, Young's modulus, coefficient of linear expansion and Poisson's ratio, respectively. R represents the maximum allowable temperature difference. These parameters could be used to evaluate the cracking sensitivity of crucibles after erosion of molten alloys. Table 5 lists the calculated R values of $BaZrO_3$ and Y_2O_3. All data in Table 5 are derived from Ref. [9]. The σ_f value is cold modulus of rupture value. The α value ranges from room temperature to 1200 °C. It can be seen that $BaZrO_3$ and Y_2O_3 possessed similar intrinsic physical properties such as strength, Young's modulus, coefficient of linear expansion and Poisson's ratio. Therefore, for the Y50 crucible, using the mixing rule, $BaZrO_3$ and Y_2O_3 were more easily combined with each other. The similar maximum allowable temperature difference (R) ensured that no cracks occurred between $BaZrO_3$ and Y_2O_3 in the melting process of the Y50 crucible, thus showing a good thermal shock resistance. In conclusion, the excellent thermodynamic stability and thermal shock resistance of the Y50 crucible made it a promising application in VIM of highly reactive titanium alloys.

Table 5. Calculated R values of $BaZrO_3$ and Y_2O_3.

Materials	σ_f (MPa)	E (GPa)	α ($\times 10^{-6}$/°C)	ν	R (°C)
$BaZrO_3$	128	181	7.6	0.258	69.04
Y_2O_3	122	181.4	8.9	0.299	52.97

4. Conclusions

In this paper, the $BaZrO_3$-Y_2O_3 two-phase crucibles were prepared, and their performance for melting Ti_2Ni alloys was evaluated by comparing with the pure $BaZrO_3$ and Y_2O_3 crucibles, respectively. The main conclusions were summarized as follows:

(1) After sintering, the $BaZrO_3$-Y_2O_3 two-phase crucibles consisted of $BaZr_{1-x}Y_xO_{3-\delta}$ and $Y_2O_3(ZrO_2)$ phases due to the mutual substitution of Zr^{4+} and Y^{3+} ions. The density of two-phase crucibles was significantly increased with the increase of Y_2O_3 addition. When Y_2O_3 addition reached 50 wt.%, the Y50 crucible had the highest densification, and its porosity was only 1.2 ± 0.3%.

(2) After melting Ti_2Ni alloys, the Y50 crucible exhibited the best erosion resistance to alloy melt with a 7 µm thick erosion layer. In addition, this crucible could introduce the least element and inclusion contamination to alloy melts.

The concentration of O, Zr, and Y elements in alloys was 0.11, 0.05 and 0.13 wt.% after third melting, respectively. This crucible had better thermodynamic stability and thermal shock resistance, indicating that it was a promising candidate for the achievement of VIM of highly reactive titanium alloys.

Acknowledgments

This work was supported by the National Key Research and Development Program (2022YFB3404500), National Natural Science Foundation of China (No. 52104305, 12305374, 52374360 and U2341267). Additionally, we thank the anonymous referee of this paper for their constructive suggestions.

Author Contributions

Conceptualization, C.L. (Chonghe Li) and G.C.; Methodology, P.G.; Software, Q.F.; Validation, P.G.; Formal Analysis, E.W.; Investigation, Q.F. and S.D.; Resources, G.C. and H.L.; Data Curation, S.D. and C.L. (Chenxi Liu); Writing—Original Draft Preparation, Q.F.; Writing—Review & Editing, C.L. (Chonghe Li), X.H. and G.C.; Visualization, H.L.; Supervision, E.W.; Project Administration, C.L. (Chonghe Li) and G.C.; Funding Acquisition, C.L. (Chonghe Li) and X.H.

Ethics Statement

Not applicable.

Informed Consent Statement

Not applicable.

Funding

This research received no external funding.

Declaration of Competing Interest

The authors declare that they have no known competing financial interests or personal relationships that could have appeared to influence the work reported in this paper.

References

1. Zhao QY, Sun QY, Xin SW, Chen YN, Wu C, Wang H, et al. High-strength titanium alloys for aerospace engineering applications: A review on melting-forging process. *J. Mater. Sci. Eng. A* **2022**, *845*, 143260.
2. Feng QS, Lv MR, Mao L, Duan BB, Yang YC, Chen GY, et al. Research progress of titanium sponge production: A review. *Metals* **2023**, *13*, 408.
3. Zhang LC, Chen LY. A review on biomedical titanium alloys: Recent progress and prospect. *Adv. Eng. Mater.* **2019**, *21*, 1801215.
4. Cui CX, Hu BM, Zhao LC, Liu SJ. Titanium alloy production technology, market prospects and industry development. *Mater. Des.* **2011**, *32*, 1684–1691.
5. Guther V, Allen M, Klose J, Clemens H. Metallurgical processing of titanium aluminides on industrial scale. *Intermetallics* **2018**, *103*, 12–22.
6. Barbosa J, Ribeiro CS, Monteiro AC. Influence of superheating on casting of γ-TiAl. *Intermetallics* **2007**, *15*, 945–955.
7. Sung SY, Kim YJ. Economic net-shape forming of TiAl alloys for automotive parts. *Intermetallics* **2006**, *14*, 1163–1167.
8. Weber BC, Thompson WM, Bielstein HO, Schwartz MA. Ceramic crucible for melting titanium. *J. Am. Ceram. Soc.* **1957**, *40*, 363–373.
9. Wang RY, Zhao C, Liu XT, Sun MH, Li N. Anti-corrosion AlN ceramic crucible with excellent thermal shock resistance for induction melting of TiAl alloy. *Ceram. Int.* **2023**, *49*, 35679–35686.
10. Cui RJ, Tang XX, Gao M, Zhang H, Gong SK. Thermodynamic analysis of interactions between Ti-Al alloys and oxide ceramics. *Trans. Nonferrous Met. Soc. China* **2012**, *22*, 887–894.
11. Ren P, Wang XG, Zhang M, Sun XD. Fabrication of yttrium oxide refractory with high strength and thermal shock stability for smelting TiAl alloy. *Ceram. Int.* **2024**, *50*, 464–473.
12. Li HR, Liu Y, Yang JJ, Yuan M, Sun AL, Lin TS, et al. Preparation and application evaluation of La_2O_3-doped Y_2O_3 crucible materials for melting TiAl alloys. *Ceram. Int.* **2022**, *48*, 15762–15769.

13. Schaffoner S, Aneziris CG, Berek H, Rotmann B, Friedrich B. Investigating the corrosion resistance of calcium zirconate in contact with titanium alloy melts. *J. Eur. Ceram. Soc.* **2015**, *35*, 259–266.
14. Li ZY, Fu L, Zou YS, Gu HZ, Huang A, Chen D, et al. A novel potential ceramic material for melting Ti6Al4V alloy: A solid solution of $BaZrO_3$ and $CaZrO_3$. *J. Eur. Ceram. Soc.* **2023**, *43*, 6571–6580.
15. Meng DZ, Chen GY, Zhang RL, Li CH. Preparation of Y_2O_3 doped $SrZrO_3$ refractory and study on its interface reaction with molten TiNi alloys. *Key Eng. Mater.* **2018**, *768*, 256–260.
16. Qiu SH, Li ML, Shao G, Wang HL, Zhu JP, Liu W, et al. $(Ca,Sr,Ba)ZrO_3$: A promising entropy-stabilized ceramic for titanium alloys smelting. *J. Mater. Sci. Technol.* **2021**, *65*, 82–88.
17. Gao PY, Liu YZ, Ren Y, Chen GY, Lan BB, Lu XG, et al. Evaluation of the microstructure and property of TiNi SMA prepared using VIM in $BaZrO_3$ crucible. *Vacuum* **2019**, *168*, 108843.
18. He J, Wei C, Li M, Wang H, Lu XG, Li CH. Interface reaction between $BaZrO_3$ refractory and melted TiAl alloys. *Chin. J. Nonferrous Met.* **2015**, *25*, 1505–1511.
19. Chen GY, Lan BB, Xiong FH, Gao PY, Zhang H, Lu XG, et al. Pilot-scale experimental evaluation of induction melting of Ti-46A1-8Nb alloy in the fused $BaZrO_3$ crucible. *Vacuum* **2019**, *159*, 293–298.
20. Chen GY, Cheng ZW, Wang SS, Qin ZW, Lu XG, Li CH. Interfacial reaction between high reactivity titanium melt and $BaZrO_3$ refractory. *J. Chin. Ceram. Soc.* **2016**, *44*, 890–895.
21. Chen GY, Gao PY, Kang JY, Li BT, Ali W, Qin ZW, et al. Improved stability of $BaZrO_3$ refractory with Y_2O_3 additive and its interaction with titanium melts. *J. Alloys Compd.* **2017**, *726*, 403–409.
22. Kang JY, Chen GY, Lan BB, Zhang RL, Ali W, Lu XG, et al. Sintering behavior of Y-doped $BaZrO_3$ refractory with TiO_2 additive and effects of its dissolution on titanium melts. *Int. J. Appl. Ceram. Technol.* **2019**, *16*, 1088–1097.
23. Chen GY, Yu FH, Hou X, Yang YC, Duan BB, Feng QS, et al. Performance of $BaZrO_3/Y_2O_3$ dual-phase refractory applied to TiAl alloy melting. *Ceram. Int.* **2022**, *48*, 20158–20167.
24. Hou X, Chen GY, Liu J, Lv MR, Yu FH, Feng QS, et al. Interaction mechanism between $BaZrO_3/Y_2O_3$ refractory and Ti_2Ni alloy melts. *J. Iron Steel Res. Int.* **2023**, *31*, 1376–1388.
25. Iwashita N. X-ray powder diffraction. *Mater. Sci. Eng. Carbon Charact.* **2016**, 7–25. doi:10.1016/B978-0-12-805256-3.00002-7.
26. Available online: http://abulafia.mt.ic.ac.uk/shannon/ptable.php (accessed on 10 August 2024).
27. Han DL, Uda T. The best composition of an Y-doped $BaZrO_3$ electrolyte: Selection criteria from transport properties, microstructure, and phase behavior. *J. Mater. Chem. A* **2018**, *6*, 18571–18582.
28. Lin CM, Wang SS, Chen GY, Wang K, Cheng ZW, Lu XG, et al. Thermodynamic evaluation of the $BaO\text{-}ZrO_2\text{-}YO_{1.5}$ system. *Ceram. Int.* **2016**, *42*, 13738–13747.
29. Lee JH, Gan ZH, Han OH. Effect of Ba nonstoichiometry in $Ba_x(Zr_{0.8}Y_{0.2})O_{3-\delta}$ on population of 5-coordinated Y. *J. Am. Ceram. Soc.* **2014**, *97*, 3749–3754.
30. Chen GY, Kang JY, Gao PY, Qin ZW, Lu XG, Li CH. Dissolution of $BaZrO_3$ refractory in titanium melt. *Int. J. Appl. Ceram. Technol.* **2018**, *15*, 1459–1466.
31. Gomes F, Puga H, Barbosa J, Ribeiro CS. Effect of melting pressure and superheating on chemical composition and contamination of yttria-coated ceramic crucible induction melted titanium alloys. *J. Mater. Sci.* **2011**, *46*, 4922–4936.
32. Zou L, Guo CP, Li CR, Du ZM. Experimental investigation and thermodynamic modeling of the Ni-Ti-V system. *Calphad* **2019**, *64*, 97–114.
33. Cui RJ, Gao M, Zhang H, Gong SK. Interactions between TiAl alloys and yttria refractory material in casting process. *J. Mater. Process. Technol.* **2010**, *210*, 1190–1196.
34. Mandal S, Kumar CJD, Kumar D, Syed K, Ende MAV, Jung IH, et al. Designing environment-friendly chromium-free Spinel-Periclase-Zirconia refractories for Ruhrstahl Heraeus degasser. *J. Am. Ceram. Soc.* **2020**, *103*, 7095–7114.
35. Sadrnezhaad SK, Raz SB. Interaction between refractory crucible materials and the melted NiTi shape-memory alloy. *Metall. Mater. Trans. B* **2005**, *36*, 395–403.
36. Liu YS, Gao YY, Wang EH, Chen GY, Xu EX, Zhao F, et al. Interaction between CA6-MA crucible and molten wrought Ni-based superalloys. *J. Eur. Ceram. Soc.* **2023**, *43*, 1714–1722.
37. Fashu S, Lototskyy M, Davids MW, Pickering L, Linkov V, Tai S, et al. A review on crucibles for induction melting of titanium alloys. *Mater. Des.* **2020**, *186*, 108295.
38. Kingery WD. Factors affecting thermal stress resistance of ceramic materials. *J. Am. Ceram. Soc.* **1955**, *38*, 3–15.
39. Swain MV. R-curve behavior and thermal shock resistance of ceramics. *J. Am. Ceram. Soc.* **1990**, *73*, 621–628.